

The sky distribution of positronium annihilation continuum emission measured with SPI/INTEGRAL^{*}

G. Weidenspointner^{1**}, C.R. Shrader², J. Knödlseher¹, P. Jean¹, V. Lonjou¹, N. Guessoum³, R. Diehl⁴, W. Gillard¹, M.J. Harris¹, G.K. Skinner¹, P. von Ballmoos¹, G. Vedrenne¹, J.-P. Roques¹, S. Schanne⁵, P. Sizun⁵, B.J. Teegarden², V. Schönfelder⁴, and C. Winkler⁶

¹ Centre d'Etude Spatiale des Rayonnements, 9 Avenue Colonel Roche, 31028 Toulouse Cedex 4, France

² NASA Goddard Space Flight Center, LHEA, Code 661, Greenbelt, MD 20771, USA

³ American University of Sharjah, College of Arts & Science, Physics Department, PO Box 26666, Sharjah, UAE

⁴ Max-Planck-Institut für extraterrestrische Physik, Postfach 1603, 85740 Garching, Germany

⁵ DSM/DAPNIA/SAP, CEA Saclay, 91191 Gif-sur-Yvette, France

⁶ ESA/ESTEC, Science Operations and Data Systems Division (SCI-SD), 2201 AZ Noordwijk, The Netherlands

Received ; accepted

Abstract. We present a measurement of the sky distribution of positronium (Ps) annihilation continuum emission obtained with the SPI spectrometer on board ESA's INTEGRAL observatory. The only sky region from which significant Ps continuum emission is detected is the Galactic bulge. The Ps continuum emission is circularly symmetric about the Galactic centre, with an extension of about 8° FWHM. Within measurement uncertainties, the sky distribution of the Ps continuum emission is consistent with that found by us for the 511 keV electron-positron annihilation line using SPI. Assuming that 511 keV line and Ps continuum emission follow the same spatial distribution, we derive a Ps fraction of 0.92 ± 0.09 . These results strengthen our conclusions regarding the origin of positrons in our Galaxy based on observations of the 511 keV line. In particular, they suggest that the main source of Galactic positrons is associated with an old stellar population, such as Type Ia supernovae, classical novae, or low-mass X-ray binaries. Light dark matter is a possible alternative source of positrons.

Key words. Gamma rays: observations – Galaxy: bulge

1. Introduction

The annihilation of positrons with electrons gives rise to two characteristic emissions at gamma-ray energies: the hallmark line at 511 keV, and the unique three-photon positronium (Ps) continuum emission (cf. Guessoum, Jean, & Gillard 2005). Direct annihilation of positrons with electrons, and their annihilation via the formation of para-Ps (with the spins of electron and positron being anti-parallel), result in the emission of two 511 keV photons. Annihilation via the formation of ortho-Ps (with the spins of electron and positron being parallel) produces three photons and gives rise to the Ps continuum emis-

sion, which is roughly saw-tooth shaped with a peak at the maximum energy of 511 keV (Ore & Powell 1949).

Cosmic positron annihilation radiation was first detected from the Galactic centre (GC) direction in balloon observations during the 1970s and has been the focus of intense scrutiny by a large number of balloon and satellite borne experiments ever since (see e.g. the reviews by Tueller 1992; Harris 1997). Despite tremendous observational and theoretical efforts, the origin of the positrons is still poorly understood. A large variety of positron sources and production mechanisms have been proposed over the years (e.g. Chan & Lingelfelter 1993; Dermer & Murphy 2001). Among the more promising source candidates are radioactive nucleosynthesis products from supernovae. More recently, hypernovae/GRBs (Cassé et al. 2004; Parizot et al. 2005) and light dark matter (e.g. Boehm et al. 2004) have been proposed as possible candidates. Compact objects comprise another potential candidate source of positrons.

Investigations of the sky distribution of the annihilation radiation promise to provide clues to the identi-

Send offprint requests to: G. Weidenspointner, e-mail Georg.Weidenspointner@cesr.fr

^{*} Based on observations with INTEGRAL, an ESA project with instruments and science data centre funded by ESA member states (especially the PI countries: Denmark, France, Germany, Italy, Switzerland, Spain), Czech Republic and Poland, and with the participation of Russia and the USA.

^{**} External ESA Fellow

fication of the source(s) of positrons in our Galaxy, despite the fact that positrons may travel from their birth places before annihilating. First maps of the annihilation radiation, limited to the inner regions of our Galaxy, were obtained using the OSSE instrument on board the Compton Gamma-Ray Observatory (Johnson et al. 1993) in the 511 keV line and in Ps continuum emission (e.g. Purcell et al. 1997; Chen et al. 1997; Milne et al. 2000, 2001a,b, 2002). Furthermore, the OSSE instrument allowed Kinzer et al. (1999, 2001) to study the one-dimensional distribution in longitude and in latitude of diffuse emission, including annihilation radiation, from the inner Galaxy. With the commissioning of the imaging spectrometer SPI on board ESA’s INTEGRAL observatory, high spectral resolution mapping with improved angular resolution has become feasible (Jean et al. 2003a; Weidenspointner et al. 2004; Knödlseeder et al. 2005). The 511 keV line emission is found to be dominated by the Galactic bulge and/or halo; emission from the Galactic disk is much fainter, implying that positron annihilation is concentrated in the central regions of our Galaxy (Knödlseeder et al. 2005).

A first SPI measurement of the flux in Ps continuum emission, and of the Ps fraction f_{Ps} (the fraction of positrons that annihilate through Ps formation; Brown & Leventhal 1987), has been presented by Churazov et al. (2005). The value of f_{Ps} , as well as the detailed shape of the 511 keV annihilation line, depend on the physical properties of the annihilation media; therefore detailed spectroscopy of the positron annihilation can provide unique information on the annihilation media and processes (Guessoum, Jean, & Gillard 2005; Jean et al. 2006).

In this publication, we present results concerning the Galactic distribution of Ps continuum emission using observations of most of the celestial sphere with the spectrometer SPI/INTEGRAL. The analysis of the SPI observations is presented in Sec. 2. Our mapping, model fitting, and spectral results are given in Sec. 3. A summary and our conclusions can be found in Sec. 4.

2. Instrument description and data analysis

The SPI imaging spectrometer consists of an array of 19 actively cooled high resolution Ge detectors, which cover an energy range of 20–8000 keV with an energy resolution of about 2.1 keV FWHM at 511 keV. SPI employs an active anti-coincidence shield made of bismuth germanate (BGO), which also acts as a collimator. In addition to its spectroscopic capabilities, SPI can image the sky with moderate spatial resolution of about 3° FWHM using a tungsten coded aperture mask. The fully coded field-of-view of the instrument is about 16°. A detailed description of the instrument was given by Vedrenne et al. (2003).

The analysis presented here is based on the same data set that we used to study the sky distribution of the 511 keV electron-positron annihilation line (for details see Knödlseeder et al. 2005). The data comprise all

observations included in the December 10, 2004 public INTEGRAL data release (i.e. three-day orbital revolutions 16–76, 79–80, 89–122) supplemented by instrument team observations of the Vela region during revolutions 81–88. The observations were taken during the epoch December 9, 2002 through September 12, 2003. In total, the data set consists of 6821 pointings¹ with a combined live time of 13.5×10^6 s. The resulting exposure to the sky (see Fig. 1 in Knödlseeder et al. 2005) is relatively uniform for Galactic longitudes $|l| \leq 50^\circ$ and Galactic latitudes $|b| \leq 15^\circ$, with a maximum at the GC region. Unexposed regions are limited to the south Galactic pole region and a few areas at intermediate Galactic latitudes.

The analysis of the Ps continuum emission, and of the underlying Galactic power-law continuum (hereafter: Galactic continuum) emission², is rendered challenging by a signal-to-background ratio which is only of the order of a few tenths of one per cent (compared to a few per cent for the 511 keV annihilation line). Background modelling therefore is crucial. Our approach consists of fitting time series of detector count rates by a linear combination of so-called background templates (time series of background components, explained below). The detector signal arising from a celestial source is also variable in time, even if the source is intrinsically stable, because SPI’s exposure to it varies in time as the instrument performs a series of observations. Source components can be distinguished from the dominant background components by taking advantage of their differing time series.

Many processes contribute to the instrumental background at all energies (Jean et al. 2003b; Weidenspointner et al. 2003). The statistical significance of the available data is still a limiting factor in the analysis of sky signals. We found that the background components used by Knödlseeder et al. (2005) to model the instrumental 511 keV line provide a viable compromise between accuracy and simplicity. The model consists of three components: a constant, the rate of saturating (> 8 MeV) events in the Ge detectors, and a template representing the exponential build-up of long-lived isotopes (a lifetime of 352 days, corresponding to ^{65}Zn , was chosen³). The role of the first two templates is to account for prompt and short-lived background components,

¹ Each INTEGRAL observation is split into numerous so-called pointings, often arranged on a square grid of 25 positions on the sky centred on the main target of the observation, which each pointing lasting about 2000 s (Courvoisier et al. 2003). This so-called dithering strategy is necessary to minimize imaging artefacts for SPI by providing a sufficient number of measurements (sky signal and instrumental background) for each of the 19 detectors to constrain sufficiently the fluxes from each pixel in the field-of-view.

² This emission is partly due to cosmic-ray interactions in the interstellar medium, partly due to point sources.

³ Since our data extend only over about 1 year, we cannot yet distinguish different half-lives longer than about 6 months. The exact value of the lifetime is therefore not crucial, but it is important to allow for the significant long-term build-up effect.

the third template accounts for long-lived background components. This three-component background model was applied either separately to three energy intervals, namely 410–430, 447–465, and 490–500 keV (hereafter: Ps analysis intervals), or to the summation of the events in these three intervals into a single data set (hereafter: summed Ps analysis intervals). The intervals were chosen to be free of strong background features (which require specific modelling using other, intermediate time scales). We do not include the fourth background component used in the 511 keV line analysis, which represented the continuum underlying the instrumental 511 keV line. Thus we are measuring the total emission, Ps continuum plus Galactic continuum.

As in studies of the sky distribution of the 511 keV line emission, we found that by fitting the normalizations of each of the three background model components for each detector remaining systematic uncertainties introduce a bias. However, if we fit the second background component not only for each SPI detector, but additionally for each orbital revolution (as in model ORBIT-DETE in Knödlseider et al. 2005) we reduce systematic trends to an acceptable level. This method is similar to those applied by us in earlier analyses of the 511 keV line (e.g. Jean et al. 2003a; Knödlseider et al. 2003; Weidenspointner et al. 2004).

To obtain model independent maps of extended emission from our Galaxy we employed an implementation of the Richardson-Lucy algorithm that is described in detail in Knödlseider et al. (2005). Briefly, in this approach the intensity attributed to each sky pixel is calculated iteratively using the relation

$$f_j^{k+1} = f_j^k + \lambda^k \omega_j f_j^k \left(\frac{\sum_{i=1}^N \left(\frac{n_i}{e_i^k} - 1 \right) R_{ij}}{\sum_{i=1}^N R_{ij}} \right) \quad (1)$$

where k is the iteration number, f_j^k is the intensity from sky pixel j in iteration k , R_{ij} is the instrumental response matrix (linking data space bin i to sky pixel j), n_i is the number of counts measured in data space bin i , $e_i^k = \sum_{j=1}^M R_{ij} f_j^k + b_i$ is the predicted number of counts in data space bin i after iteration k (with b_i being the predicted number of instrumental background counts for data space bin i), N and M are the dimensions of the data and image spaces, respectively, and λ^k is an acceleration factor. To avoid noise artefacts in weakly exposed regions of the sky, the image increments are weighted with a quantity $\omega_j = (\sum_{i=1}^N R_{ij})^2$ that is related to the sensitivity of the instrument.

When fitting models of intensity distributions on the sky to the data, we employed the maximum likelihood multi-component model fitting algorithm described in detail in Knödlseider et al. (2005). Briefly, assuming Poisson noise for the measured number n_i of events in each of

the N data space bins, the algorithm maximizes the log likelihood function

$$\ln L = \sum_{i=1}^N n_i \ln e_i - e_i - \ln n_i! \quad (2)$$

where $e_i = \sum_k \alpha_k s_i^k + b_i(\boldsymbol{\beta})$ is the predicted number of (source plus background) counts in data space bin i , $s_i^k = \sum_{j=1}^M f_j^k R_{ij}$ is the sky intensity model k folded into data space bin i (with f_j^k being the intensity in sky pixel j due to sky model k and R_{ij} being the instrumental response matrix), $b_i(\boldsymbol{\beta})$ is the background model, and α_k and $\boldsymbol{\beta}$ are scaling factors for the sky intensities and the background model components, respectively, that are adjusted by the fit.

3. Results

3.1. Mapping

We employed an implementation of the Richardson-Lucy algorithm, outlined in Sec. 2, to obtain a model independent map of the extended emission in the summed Ps analysis intervals (i.e. the events were first summed and then analyzed, hence the total emission in the three energy intervals is mapped without constraints on the relative fluxes in each of them; spectroscopy of the emission is presented in Sec. 3.3). Since we are only interested in extended emission, the two point sources Crab and Cygnus X-1 (which are clearly seen due to their strong continuum emission at these energies) were subtracted in the image reconstruction process. In addition, to reduce noise artefacts, the iterative corrections were smoothed during image reconstruction with a $5^\circ \times 5^\circ$ boxcar average. The resulting sky map after iteration 8 is presented in Fig. 1. We selected this iteration because at this point of the iterative mapping procedure the fit quality corresponds approximately to that which we obtained when fitting sky models to the data (see Sec. 3.2). This choice ensures that the algorithm has not yet overfitted the data, which could result in substantial image noise and image artefacts. We note, however, that analyses of simulated observations show that at this point in the iterations and with the limited amount of data available, features such as the faint extended emission expected from the Galactic plane would not necessarily be apparent, and indeed the Galactic plane is not apparent in Fig. 1 although we detect it at a low significance level in model fits (see Sec. 3.2). The simulations also show that with increasing iterations (in our analysis beyond iteration 8) faint extended emission begins to appear, however, so do artefacts due to overfitting, and a distinction in the image between actual signal and noise becomes increasingly difficult.

The only prominent signal seen is that from the Galactic bulge region. The surface brightness of any emission from any other sky regions is much fainter. The emission appears to be symmetric about the GC, and its centroid coincides well with the GC. In short, the characteristics of the extended emission in the three Ps analysis

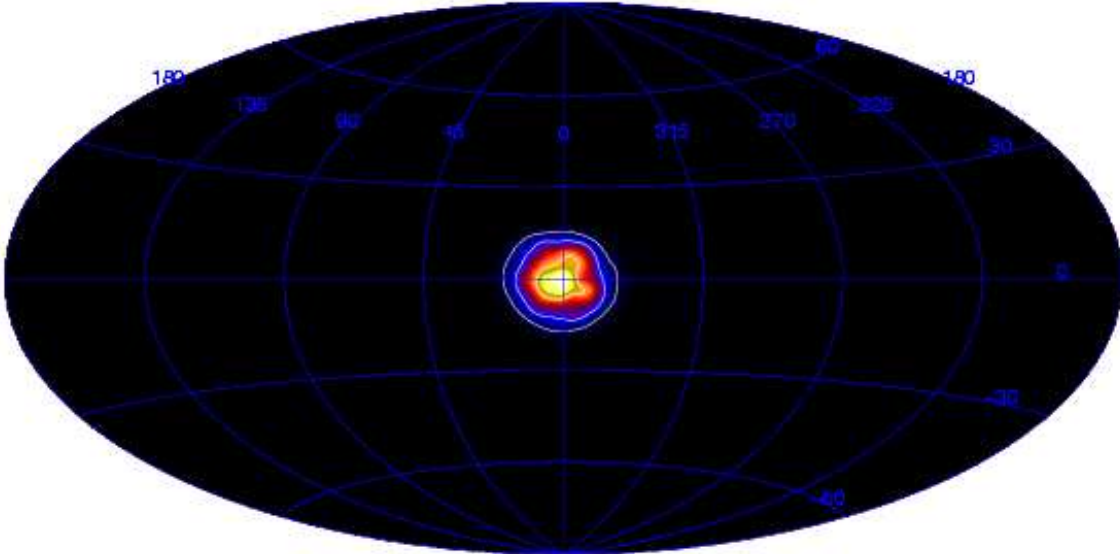


Fig. 1. A Richardson-Lucy sky map of extended emission in the summed Ps analysis intervals (the combination of the intervals 410–430, 447–465, and 490–500 keV). The contour levels indicate intensity levels of 10^{-2} , 10^{-3} , and 10^{-4} ph cm $^{-2}$ s $^{-1}$ sr $^{-1}$. Details are given in the text.

intervals agree well with those already identified by us for the 511 keV line radiation. This agreement suggests that the extended emission from the GC region in the Ps analysis intervals is dominated by Ps continuum emission, with the Galactic continuum emission being fainter (as will be demonstrated in Sec. 3.3). We note that these characteristics are consistent with OSSE maps obtained for the Ps continuum emission (e.g. Milne et al. 2001b, 2002), in which the surface brightness is highest in the bulge.

We also used the SPIROS algorithm (Skinner & Connell 2003) to search for point sources in these three energy bands. No significant sources in addition to the Crab and Cygnus X-1 were found outside the GC region. When imaging the GC region with SPIROS, the observed emission formally is equally well explained by six point sources. However, different sets of sources are found in the different Ps analysis intervals. These sources do not coincide with any known high-energy sources, including the four highest energy sources reported by Bouchet et al. (2005). The spectrum of these four sources drops steeply above about 300 keV, and since we are analyzing rather narrow energy intervals above 400 keV the fact that we do not yet detect them is not surprising. We therefore conclude that the point sources found by us using SPIROS are all spurious, resulting from SPIROS’ attempt to account for intrinsically diffuse emission with a set of point sources.

3.2. Model fitting

A more quantitative approach for studying the Galactic distribution of the observed extended emission is model fitting, which we performed using a maximum likelihood

multi-component fitting algorithm (Knödlseeder et al. 2005) outlined in Sec. 2.

We first modelled the emission in the three summed Ps analysis intervals⁴ by an ellipsoidal distribution with a Gaussian radial profile and determined the best-fit centroid location (l_0, b_0) and extent in Galactic longitude and latitude ($\text{FWHM}_l, \text{FWHM}_b$). We then combined this Galactic bulge model with one of two models for emission from the Galactic disk: both HI (Dickey & Lockman 1990) and CO (Dame et al. 1987) distributions are tracers of Galactic matter and are believed to correlate with diffuse emission (cf. Harris et al. 1990; Kinzer et al. 1999; Strong et al. 2004). The results of these fits are summarized in Table 1. In each of these fits, the Crab and Cygnus X-1 were included as steady point sources whose intensities were fitted. When including the four highest-energy sources reported by Bouchet et al. (2005) the quality of the fits is only slightly improved and the fit results do not change significantly; therefore these point sources were excluded from the final analysis.

As can be seen from Table 1, the centroid of the bulge emission is the same within errors for all three models. There is marginal evidence for a slight offset of the centroid from the GC, but it is of a magnitude that could easily result from the combined effects of statistical and systematic biases in the background model (indeed, there is a similarly marginal, but opposite, offset of the centroid in the 511 keV line emission; Knödlseeder et al. 2005). The extent of the bulge emission, and its flux, do depend on the sky model. If the extended emission is modelled by a bulge component only, then there is marginal evidence for the bulge emission to be more extended in longitude than in

⁴ Results for the individual energy intervals are consistent within statistical uncertainties.

Table 1. A summary of results from model fitting in the summed Ps analysis intervals (the combination of the intervals 410–430, 447–465, and 490–500 keV). In the table, λ is the maximum likelihood ratio of the fit, f_b , f_{HI} , and f_{CO} are the fluxes in the bulge and the two different disk components, respectively. The remaining symbols are defined in the text. The error bars reflect the statistical 1σ confidence interval for one degree of freedom.

Quantity	Value
Bulge only	
λ	494.5
l_0 [°]	1.3 ± 0.8
b_0 [°]	-0.8 ± 0.6
FWHM_l [°]	$10.0^{+4.1}_{-1.9}$
FWHM_b [°]	$6.6^{+1.4}_{-1.2}$
ϵ	$0.66^{+0.22}_{-0.20}$
f_b [ph/cm ² /s]	$1.20^{+0.14}_{-0.11} \times 10^{-3}$
Bulge + HI	
λ	502.2
l_0 [°]	1.3 ± 0.8
b_0 [°]	-0.9 ± 0.6
FWHM_l [°]	$9.3^{+2.6}_{-1.5}$
FWHM_b [°]	$6.8^{+1.5}_{-1.2}$
ϵ	$0.71^{+0.26}_{-0.20}$
f_b [ph/cm ² /s]	$1.16^{+0.12}_{-0.10} \times 10^{-3}$
f_{HI} [ph/cm ² /s]	$4.19^{+1.52}_{-1.53} \times 10^{-3}$
Bulge + CO	
λ	510.5
l_0 [°]	1.3 ± 1.1
b_0 [°]	-1.2 ± 1.0
FWHM_l [°]	$9.2^{+3.1}_{-2.1}$
FWHM_b [°]	$7.8^{+3.2}_{-1.7}$
ϵ	$0.85^{+0.44}_{-0.27}$
f_b [ph/cm ² /s]	$0.86^{+0.15}_{-0.13} \times 10^{-3}$
f_{CO} [ph/cm ² /s]	$1.92^{+0.49}_{-0.48} \times 10^{-3}$

latitude (the ellipticity $\epsilon \equiv \text{FWHM}_b/\text{FWHM}_l$ deviates by about 1.5σ from unity). However, inclusion of a Galactic disk component improves the fits, with the significances of the HI distribution and of the CO distribution being about 2.8σ and 4.0σ , respectively, favouring the latter. Another reason to adopt the CO distribution as the better disk model of the two is the fact that the resulting total sky flux of about $(2.8 \pm 0.5) \times 10^{-3}$ ph cm⁻² s⁻¹ agrees well with the value of about 2.5×10^{-3} ph cm⁻² s⁻¹ determined with SMM⁵ in the Ps analysis intervals, whereas the total bulge and HI disk model flux of $(5.4 \pm 1.5) \times 10^{-3}$ ph cm⁻² s⁻¹ is only marginally consistent with the SMM spectrum of Harris et al. (1990).

Inclusion of a Galactic disk component in the fits also renders evidence for ellipticity of the bulge component

insignificant. The bulge shape is consistent with circular symmetry, with a FWHM of about 8° , in agreement with our results for the 511 keV line (Knödlseher et al. 2005). As is the case for the annihilation line, the extent of the Ps continuum bulge emission is slightly larger than that derived by Kinzer et al. (2001) from OSSE observations. However, the difference is not very significant, and it is possible that there is bias in the OSSE analysis favouring a smaller bulge extent (Kinzer et al. 2001).

The fluxes that are attributed to the disk components exceed the bulge flux by factors of 2–4 (see Table 1). However, since the disk flux is distributed over a much larger sky region, the corresponding surface brightness is much lower. The model fits therefore confirm the mapping result: the intensity of extended Galactic emission in the three Ps analysis intervals is brightest in a region, several degrees across, around the GC.

3.3. Spectral analysis

To assess the relative contributions of Ps continuum and Galactic continuum emission to the emission mapped in Fig. 1, we performed a spectral analysis in six energy intervals: the three bands used for the Ps continuum analysis supplemented by the energy intervals 500–507, 507–515, and 515–565 keV. More detailed spectroscopy including the line shape is presented in Jean et al. (2006). We want to emphasize that present uncertainties in the sky distribution of the emission components, in particular for the Galactic continuum emission, imply systematic uncertainties for this kind of spectral analysis. Similarly, when comparing different results, one has to keep in mind that there will be a systematic difference between fluxes obtained under different assumptions for the spatial distribution of the emission.

3.3.1. Simplistic SPI spectroscopy

A first, and rather simplistic, spectral analysis of the SPI result for the diffuse emission from the GC region ($|l|, |b| \leq 16^\circ$) was performed by fitting three spectral components: a line at 511 keV, the Ps continuum, and a power law⁶ representing the Galactic continuum. Before fitting, these models were convolved with the SPI instrumental resolution. Following our best sky model (“Bulge+CO”, see Table 1), and in agreement with our results on the sky distribution of the 511 keV line emission, the SPI fluxes used in this fit were obtained assuming that the bulge emission is circularly symmetric about the GC with a Gaussian radial profile and a FWHM of 8° , and assuming that the disk emission is traced by the line-of-sight integrated CO distribution (hereafter: model G8CO).

The limited data available for this spectral analysis required that some parameters of our spectral model be fixed or constrained. The centroid and width of the astrophys-

⁵ The Gamma Ray Spectrometer on board the Solar Maximum Mission (Forrest et al. 1980).

⁶ The power law is defined as $f_{\text{pl}}(E) = A \cdot (E/300 \text{ keV})^{-\alpha}$

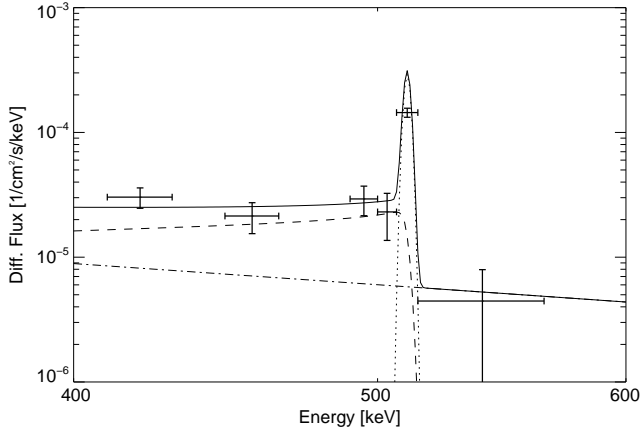


Fig. 2. A fit of the SPI result for the diffuse emission from the GC region ($|l|, |b| \leq 16^\circ$) obtained with a spatial model consisting of an 8° FWHM Gaussian bulge and a CO disk. In the fit a diagonal response was assumed. The spectral components are: 511 keV line (dotted), Ps continuum (dashes), and power-law continuum (dash-dots). The summed models are indicated by the solid line. Details of the fitting procedure are given in the text.

ical positron annihilation line were fixed at 511 keV and 2.5 keV FWHM (c.f. Lonjou et al. 2004; Churazov et al. 2005), respectively. In addition, the power-law photon index α was fixed at 1.75 (c.f. Kinzer et al. 1999; Bouchet et al. 2005). In this first analysis, off-diagonal elements in the SPI response, which are small, were neglected. When fitting the spectral models to the data, the models were averaged over the energy intervals pertaining to each data point. A rigorous spectral analysis, using the full response matrix of SPI, will be presented below. The advantage of this first analysis is its simplicity, and the fact that its results can easily be displayed graphically.

The best fit result is shown in Fig. 2. We find a 511 keV line flux of $(1.02 \pm 0.10) \times 10^{-3}$ ph cm $^{-2}$ s $^{-1}$, and a Ps continuum flux of about $(5.41 \pm 1.59) \times 10^{-3}$ ph cm $^{-2}$ s $^{-1}$. From these fluxes, and using simple error propagation, we obtain a value of f_{Ps} of 1.04 ± 0.07 for the Ps fraction as defined by Brown & Leventhal (1987). The power law is not significantly detected with a normalization of $(1.47 \pm 0.93) \times 10^{-5}$ ph cm $^{-2}$ s $^{-1}$ keV $^{-1}$. The χ^2 of the fit is about 1.8 for 3 degrees of freedom. Based on the best fit parameter values, the Ps continuum emission accounts for about 71% of the total emission in the three Ps continuum analysis intervals mapped in Fig. 1.

3.3.2. Rigorous SPI spectroscopy

To perform a rigorous spectral analysis of the emission from the Galactic bulge, we fitted the same spectral model – a line at 511 keV, the Ps continuum, and a power law – to a grid of points centred on the GC using the INTEGRAL/SPI specific capabilities of the XSPEC (ver 12) analysis package (see e.g. Dorman & Arnaud 2001), which allowed us to take into account the full spectral

and spatial response of the instrument. For a detailed description of this methodology the reader is referred to Shrader et al. (2004); here we will just briefly describe the basic procedure followed. This is the first time that XSPEC has been applied to spectroscopy of an extended sky source observed with the SPI instrument. As an aside note, we wish to warn the interested reader that we found the original Ps continuum model in XSPEC, POSM, to be incorrectly implemented. We developed and tested a new implementation of the Ore & Powell (1949) spectral shape of Ps continuum emission, which will be included in subsequent releases of XSPEC.

The data selected for this portion of our analysis comprise a subset of the total data presented in this paper. Observations were selected for inclusion in our spectral fitting when the SPI telescope axis was aligned with the GC to within an angular offset of 16° (the extent of the nominal fully-coded SPI field-of-view). This resulted in a total of about 750 spacecraft pointings (Science Windows), totalling ~ 1.7 Ms of live time, being used in this analysis.

The full SPI instrument response, including diagonal plus off-diagonal matrix elements, was then computed, according to the methodologies described in Sturmer et al. (2003), for each SPI detector for each selected instrument pointing for each of our grid points spatially sampling the bulge region. Specifically, we computed the response for a 21-point raster at $(l, b) = (0^\circ, 0^\circ), (\pm 4^\circ, 0^\circ), (0^\circ, \pm 4^\circ), (\pm 8^\circ, 0^\circ), (0^\circ, \pm 8^\circ), (\pm 4^\circ, \pm 4^\circ), (\pm 8^\circ, \pm 4^\circ), (\pm 4^\circ, \pm 8^\circ)$.

The data were then simultaneously fitted to the physical model described above – 511 keV line, Ps continuum, and power law – and the 3-component background model described in Sec. 2. The background model in this case was parameterized so that small ($\pm 10\%$) variations were allowed for the normalization terms of each component in each energy interval, using the results of model fits (as described in Sec. 3.2) to initialize the background model parameters. In practice we found that the background modelling worked quite well, with the best fit solutions typically corresponding to normalization terms within $\pm 1\%$ of unity.

We then made the assumption that the net flux consists of additive contributions from the two spatial models discussed in Sec. 3.3.1, i.e. the Gaussian and CO distributions of spatial model G8CO. The spectral model was then applied to the SPI instrument response function twice at each spatial raster, with a normalized, relative, weighting factor based on both the Gaussian and the CO distributions. This leads to a data space which scales as: (number of SPI pointings) \times (number of detectors) \times (number of spectral channels). This number is then multiplied by (number of spatial rasters) \times (2 spatial distribution models) to give the number of individual response matrices applied to the spectral model for the χ^2 minimization problem. This leads to $\sim 750 \times 19 \times 6 \times 21 \times 2 \sim 3.6 \times 10^6$ folded-model calculations per iteration step of the χ^2 minimization procedure. Specifically, we used the XSPEC “FLUX” command and the best fit parameters of each individual

model component to integrate over the covered energy range.

The parameter space was constrained as follows. The centroid and width of the positron annihilation line were fixed at 511 keV and 2.5 keV FWHM, respectively, as in our first analysis (see Sec. 3.3.1). We fixed the power-law photon index α to a value of 1.75, but allowed the amplitude to vary by about a factor of 4 relative to that obtained in our first analysis described above. Otherwise, the model parameters – specifically the Ps continuum and Gaussian line normalization terms – were allowed to vary freely in the χ^2 minimization. These two normalization terms were varied separately with respect to the two spatial distributions, but linked from grid point to grid point within a given spatial model. This leads to 6 free physical model parameters (3 normalizations for each of the 2 spatial models), in addition to the 18 background model parameters (3 parameters in each of the 6 energy intervals) for the overall fit.

We obtained a Ps continuum normalization of $(3.11 \pm 0.56) \times 10^{-3}$ ph cm $^{-2}$ s $^{-1}$. Combined with the inferred Gaussian line component normalization of $(9.35 \pm 0.54) \times 10^{-4}$ ph cm $^{-2}$ s $^{-1}$ we obtain a Ps fraction of $f_{Ps} = 0.92 \pm 0.09$. The normalization of the power-law component, rescaling the XSPEC result to the power-law function defined in footnote 6, is $(3.79^{+1.66}_{-1.25}) \times 10^{-6}$ ph cm $^{-2}$ s $^{-1}$ keV $^{-1}$. Thus over the range of our data, the power-law component contributes approximately 6% (and possibly as much as 14%) of the continuum flux based on our model fitting. If we allow the power-law index to vary freely, the resulting power-law flux remains within the confidence interval above; hence our conclusion regarding the flux contribution of the power-law component is robust. The background normalization terms, as noted, were within 1% of unity. The χ^2_{ν} value obtained was of order unity; specifically, using the full 1.65 Ms of the data selected for this analysis, a χ^2 per degree of freedom of $99065.1/86289 \approx 1.15$ was achieved. The uncertainties for a given parameter, specifically the line and Ps continuum fluxes and the power-law normalization, were derived by varying the parameter within its allowed range. At each step, the other free parameters are allowed to vary until the fit statistic is minimized, determining the 1σ confidence region for each parameter (specifically, this is accomplished using the “ERROR” procedure of XSPEC v12). We note that the uncertainty in the Ps fraction includes both the variances and the covariances of the 511 keV line and Ps continuum fluxes in the variance-covariance matrix of the fit.

Clearly, given the nature of the data and parameter spaces of the problem, it is difficult to present a graphical representation of the results. A procedure commonly used within XSPEC is to “group” the data for plotting purposes, which produces what is essentially an averaged representation of the data and model convolved with the response. In this application, however, this is not a viable option as we would be averaging over some $\sim 10^6$

spectra/responses/model calculations. We have thus chosen not to include a plot of the XSPEC results.

It follows from our spectral analysis of the Galactic bulge emission that at least 76% (the best value is 85%), of the observed flux in the summed Ps analysis intervals can be attributed to Ps continuum emission – which therefore dominates the emission from the GC region. The map in Fig. 1 is dominated by emission from the central regions of our Galaxy. Hence we can conclude that Fig. 1 provides a view of the sky distribution of Ps continuum emission.

3.3.3. Comparison to SPI results

We note that our 511 keV line flux is somewhat lower than the previous determination of $(1.05 \pm 0.06) \times 10^{-3}$ ph cm $^{-2}$ s $^{-1}$ for the Galactic bulge by Knödlseider et al. (2005) at the $\sim 2\sigma$ level (the uncertainties of other earlier SPI measurements, e.g. those by Jean et al. (2003a) or Weidenspointner et al. (2004), are too large to reach a definitive conclusion), and that the 511 keV line, the Ps continuum, and the Galactic continuum fluxes from our XSPEC analysis are lower than those obtained in our more simplistic approach described above. We suggest that this may be due to the fact that our XSPEC analysis included the off-diagonal response matrix elements, while the previous analyses used a diagonal approximation. Roughly speaking, the reason for a lower flux in our case is that with more matrix elements a smaller model flux is required to match the “model counts” with the actual detector counts in the χ^2 minimization procedure. We find for example, that for a Crab-like power-law model applied to the SPI full response leads to a $\sim 8\%$ lower flux than for the same model applied to a diagonalized version of the response. Indeed, for the actual Crab data used in determining the SPI calibration, the discrepancy between flux determinations made with SPIROS (diagonal approximation; Skinner & Connell 2003) and XSPEC was initially about 15% and in a similar sense (XSPEC flux was lower). Subsequent efforts were made to calibrate the SPIROS method for better agreement (Sizun et al. 2004). Finally, we note that the effects of the off-diagonal terms are even more pronounced for the case of a positively sloped spectrum, such as, notably, the expected Ps continuum form.

Our result for the Ps fraction of $f_{Ps} = 0.92 \pm 0.09$ agrees very well with an earlier result of $f_{Ps} = 0.96 \pm 0.06$ derived by Churazov et al. (2005) for the Galactic bulge using SPI data.

We also note that Strong et al. (2005) concluded, as we do, that the emission from the Galactic bulge is dominated by Ps continuum emission. Their results for $|l|, |b| \leq 10^\circ$ imply that about 81% of the emission in the Ps analysis intervals is due to Ps continuum emission, in excellent agreement to our result.

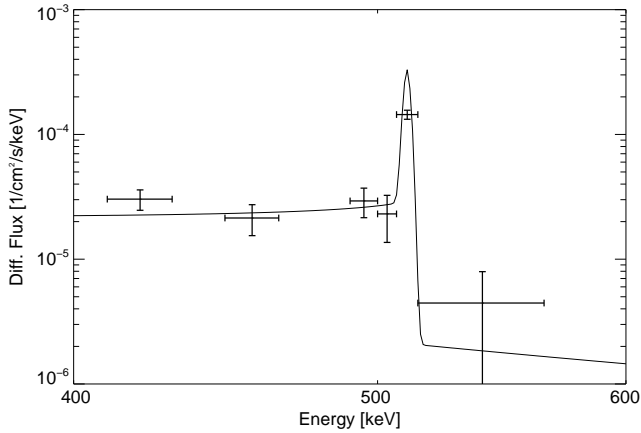


Fig. 3. A fit of the GC spectrum obtained from OSSE data by Kinzer et al. (1999) to the SPI result for the diffuse emission from the GC region ($|l|, |b| \leq 16^\circ$) obtained with a spatial model consisting of an 8° FWHM Gaussian bulge and a CO disk. Details are given in the text.

3.3.4. Comparison to OSSE results

The comparison of the astrophysical emission models determined with other instruments with our SPI results was performed by first convolving the spectral models with the SPI instrumental resolution, and then by averaging the convolved models over the energy ranges of the SPI data points. As in our spectroscopic analyses described above, the SPI results used in these comparisons were obtained with spatial model G8CO. It is worth noting that Harris et al. (1990) had assumed in their SMM analysis that the Galactic gamma-ray emission follows the CO line-of-sight distribution of Dame et al. (1987), and that Kinzer et al. (1999) had concluded from their OSSE analysis that the longitude distribution of the Galactic continuum emission follows that of CO, albeit with a somewhat broader distribution in latitude. To make comparisons with OSSE results, we consider separately the form of the spectrum, the annihilation flux, and the Galactic continuum emission.

A comparison of the Galactic spectrum seen by SPI in a box defined by $|l|, |b| \leq 16^\circ$ for our spatial model G8CO with the Kinzer et al. (1999) OSSE best fit model is depicted in Fig. 3. In this comparison of spectral forms, the normalization of the OSSE model was obtained by a fit to the SPI data. We find a normalization factor of about 0.6, and a χ^2 value of about 3.0 for 5 degrees of freedom. We conclude that the shape of the total SPI spectrum agrees well with that of the total OSSE spectrum for the GC region.

For comparison with the annihilation radiation analysis in the central square radian around the GC by Kinzer et al. (2001) using OSSE data, we repeated the simplistic spectral analysis of Sec. 3.3.1 in $|l|, |b| \leq 29^\circ$ using spatial model G8CO. Kinzer et al. (2001) obtained total annihilation radiation fluxes (i.e. the sum of the annihilation line and the Ps continuum fluxes) of about

$(6 - 11) \times 10^{-3}$ ph cm $^{-2}$ s $^{-1}$ when fitting nova ellipsoid or Gaussian bulge models combined with different thin disk models, which, of all their models, are the most similar to our G8CO model. The SPI total annihilation flux is about 7.5×10^{-3} ph cm $^{-2}$ s $^{-1}$, in very good agreement with their results. Our measurement of the Ps fraction is also in very good agreement with their value for the Galactic bulge of $f_{Ps} = 0.93 \pm 0.04$.

For the Galactic continuum emission comparison we computed the flux in the 410–500 keV band, that is most important in our analysis. Comparison with both the Kinzer et al. (2001) and the Purcell et al. (1996) analyses of OSSE observations shows good agreement. Approximating the cosmic-ray interaction model used in the Kinzer et al. (2001) analysis by a power law with photon index 1.75, we find that their results correspond to a flux of about 3.4×10^{-4} ph cm $^{-2}$ s $^{-1}$ rad $^{-1}$, whereas assuming that our results refer to a 32° range in Galactic longitude we find $3.0^{+1.3}_{-1.0} \times 10^{-4}$ ph cm $^{-2}$ s $^{-1}$ rad $^{-1}$. The Purcell et al. (1996) analysis implies a flux of about 3.6×10^{-4} ph cm $^{-2}$ s $^{-1}$ rad $^{-1}$, however, their power-law index of 2.5 is steeper than our result, which we think is due to the fact that they used data dominated by energies below a few hundred keV.

3.3.5. Comparison to SMM results

A comparison of SPI results for the diffuse emission from our Galaxy obtained with spatial model G8CO with results for the total emission from the inner Galaxy obtained from SMM data by Harris et al. (1990) (which are not essentially different from the emission from the whole Galaxy) is given in Fig. 4. As can be seen, the SPI results agree well with the best fit SMM model. Except for the 511 keV line interval our fluxes agree within their statistical 1σ errors with the Harris et al. (1990) best fit model. In the 511 keV line region our flux falls about 2σ short of the SMM result. Formally, a comparison of the SMM model to the SPI data points yields a χ^2 value of about 8.6 for 6 degrees of freedom (the model amplitude was not fitted).

4. Summary and conclusion

We studied the sky distribution of Ps continuum emission. The extent and shape of extended emission (consisting of Ps continuum and Galactic continuum) in the Ps analysis intervals between 410 and 500 keV agree well with those found for the 511 keV line by Knödlseher et al. (2005). Our bulge parameters are similar to, albeit slightly smaller than, those obtained by Kinzer et al. (2001) for the positron annihilation radiation; our Ps continuum map is bulge dominated as are the OSSE maps obtained by e.g. Milne et al. (2001b, 2002). The emission appears to be diffuse, we do not yet find evidence for significant emission in the Ps analysis intervals from point sources in the GC region. Modelling the extended emission with a Gaussian bulge of 8° FWHM located at the GC, and

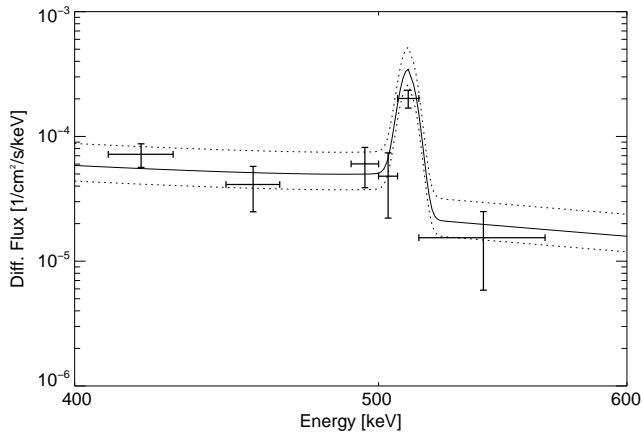


Fig. 4. Comparison of the SPI result for the diffuse emission from our Galaxy obtained with a spatial model consisting of an 8° FWHM Gaussian bulge and a CO disk (data points) with the best fit model for the emission from the inner Galaxy obtained with SMM data by Harris et al. (1990) (the solid and dashed lines represent their best fit model and its total uncertainty). Details are given in the text.

a disk component tracing the Galactic CO distribution, we derive spectra and fluxes that are consistent with previous findings obtained using SPI (Churazov et al. 2005; Knödlseeder et al. 2005), OSSE (Purcell et al. 1996; Kinzer et al. 1999, 2001), and SMM (Harris et al. 1990) observations.

Emission between 410–500 keV from around the GC region is dominated by the Ps continuum. Hence the sky distribution of Ps continuum emission and 511 keV line emission (Knödlseeder et al. 2005) are consistent, which is not surprising considering that most positrons annihilate through formation of Ps. This agreement strengthens our conclusions regarding the origin of Galactic positrons based on observations of the 511 keV line (Knödlseeder et al. 2005). In particular, our results suggest that an old stellar population, such as Type Ia supernovae, classical novae, or low-mass X-ray binaries, is the main source of Galactic positrons. Light dark matter annihilation and/or decay is another intriguing but speculative positron source.

References

- Bouchet, L., et al., 2005, *ApJ*, 635, 1103
 Boehm, C., et al., 2004, *Phys. Rev. Lett.* 92, 101301
 Brown, B.L., & Leventhal, M., 1987, *ApJ*, 319, 637
 Cassé, M., et al., 2004, *ApJ*, 602, L17
 Chan, K.-W., and Lingensfelter, R.E., 1993, *ApJ*, 405, 614
 Chen, L.X., et al., 1997, *ApJ*, 481, L43
 Churazov, E., et al., 2005, *MNRAS*, 357, 1377
 Courvoisier, T.J.-L., et al., 2003, *A&A*, 411, L53
 Dame, T.M., et al., 1987, *ApJ*, 322, 706
 Dermer, C.D., & Murphy, R.J., 2001, in *Proc. of the 4th INTEGRAL Workshop* (ESA SP-459), 115
 Dickey, J.M., & Lockman, F.J., 1990, *ARA&A*, 28, 215
 Dorman, B., & Arnaud, K.A., 2001, in *Astronomical Data Analysis Software and Systems X*, ASP Conference Proceedings 238, 415
 Forrest, D.J., et al., 1980, *Solar Phys.*, 65, 15
 Guessoum, N., Jean, P., & Gillard, W., 2005, *A&A*, 436, 171
 Harris, M.J., 1997, in *Proc. of the Fourth Compton Symposium* (AIP 410), 418
 Harris, M.J., et al., 1990, *ApJ*, 362, 135
 Jean, P., Vedrenne, G., Roques, J.-P., et al. 2003a, *A&A*, 407, L55
 Jean, P., Vedrenne, G., Roques, J.-P., et al. 2003b, *A&A*, 411, L107
 Jean, P., et al., 2006, *A&A*, 445, 579
 Johnson, W.N., 1993, *ApJS*, 86, 693
 Kinzer, R.L., Purcell, W.R., & Kurfess, J.D., 1999, *ApJ*, 515, 215
 Kinzer, R.L., et al., 2001, *ApJ*, 559, 282
 Knödlseeder, J., et al., 2003, *A&A*, 411, L457
 Knödlseeder, J., et al., 2005, *A&A*, 441, 513
 Lebrun, F., et al., 2004, *Nature*, 428, 293
 Lonjou, V., et al., 2004, in *Proc. of 5th INTEGRAL Workshop*, ESA-SP 552, 129
 Milne, P.A., et al., 2000, in *Proc. of The Fifth Compton Symposium* (AIP 510), 21
 Milne, P.A., et al., 2001a, in *Proc. of the 4th INTEGRAL Workshop 'Exploring the Gamma-Ray Universe'*, ESA SP-459, 145
 Milne, P.A., et al., 2001b, in *Proc. of Gamma 2001* (AIP 587), 11
 Milne, P.A., et al., 2002, *New Astron. Rev.*, 46, 553
 Ore, A., & Powell, J.L., 1949, *Phys. Rev.*, 75, 1696
 Parizot, E., et al., 2005, *A&A*, 432, 889
 Purcell, W.R., et al., 1996, *A&AS*, 120, 389
 Purcell, W.R., et al., 1997, *ApJ*, 491, 725
 Shrader, C.R., et al., 2004, in *Proc. of 5th INTEGRAL Workshop*, ESA-SP 552, 901
 Sizun, P., et al., 2004, in *Proc. of 5th INTEGRAL Workshop*, ESA-SP 552, 815
 Skinner, G.K., & Connell, P., 2003, *A&A*, 411, L123
 Strong, A.W., et al., 2004, in *Proc. of 5th INTEGRAL Workshop*, ESA-SP 552, 507
 Strong, A.W., et al., 2005, *A&A*, 444, 495
 Sturmer, S.J., et al., 2003, *A&A*, 411, L81
 Teegarden, B.J., et al., 2005, *ApJ*, 621, 296
 Tueller, J., 1992, in *Compton Gamma-Ray Observatory* (AIP 280), 97
 Vedrenne, G., et al., 2003, *A&A*, 411, L63
 Weidenspointner, G., et al., 2003, *A&A*, 411, L113
 Weidenspointner, G., et al., 2004, in *Proc. of 5th INTEGRAL Workshop*, ESA-SP 552, 133